HM+ and HM+-He (M = Group 2 metal): Chemical or physical interactions?

Joe P. Harris, Hannah Dodson, W. H. Breckenridge, and Timothy G. Wright

Citation: The Journal of Chemical Physics **141**, 094306 (2014); doi: 10.1063/1.4894227

View online: http://dx.doi.org/10.1063/1.4894227

View Table of Contents: http://scitation.aip.org/content/aip/journal/jcp/141/9?ver=pdfcov

Published by the AIP Publishing

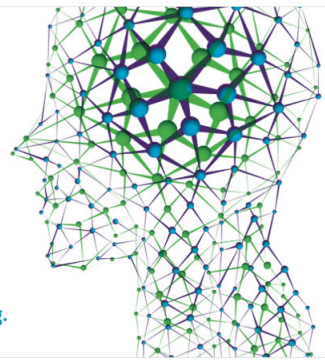

HM^+ and HM^+–He (M = Group 2 metal): Chemical or physical interactions?

Joe P. Harris,[1] Hannah Dodson,[1] W. H. Breckenridge,[2] and Timothy G. Wright[1,a)]
[1]*School of Chemistry, University of Nottingham, University Park, Nottingham NG7 2RD, United Kingdom*
[2]*Department of Chemistry, University of Utah, Salt Lake City, Utah 84112, USA*

(Received 15 July 2014; accepted 18 August 2014; published online 4 September 2014)

We investigate the HM^+–He complexes (M = Group 2 metal) using quantum chemistry. Equilibrium geometries are linear for M = Be and Mg, and bent for M = Ca–Ra; the explanation for this lies in the differing nature of the highest occupied molecular orbitals in the two sets of complexes. The difference primarily occurs as a result of the formation of the H–M^+ bond, and so the HM^+ diatomics are also studied as part of the present work. The position of the He atom in the complexes is largely determined by the form of the electron density. HM^+...He binding energies are obtained and are surprisingly high for a helium complex. The HBe^+...He value is almost 3000 cm^{-1}, which is high enough to suspect contributions from chemical bonding. This is explored by examining the natural orbital density and by population analyses. © *2014 AIP Publishing LLC*. [http://dx.doi.org/10.1063/1.4894227]

I. INTRODUCTION

Although there has been interest in trying to form chemically bonded helium for many years (see, for example, Ref. 1), there has been significant renewed interest in trying to establish if it is possible to synthesise the first stable helium-containing molecule, with molecules containing coinage metal halides currently being the most promising.[2–5] Interestingly, for these coinage metal halide complexes, the binding energy of helium was greater than neon in the respective molecules, although argon was more strongly bound than both neon and helium; the NeAuF complex has now been identified experimentally.[6,7] The binding energy of a helium atom was greatest in HeCuF, at 2270 cm^{-1}, and a small amount of covalency was deduced.[2,4] In part, the fluorine atom acts to pull electron density towards itself, thus facilitating partial donation of 1*s* electron density into the virtual Cu orbitals from the incoming He atom, leading to the designation of these as a new type of weak interaction.[3]

Grandinetti and co-workers have explored beryllium-containing ions as possible candidates for producing chemically bound helium atoms in $XBeHe^+$ species, where a number of X groups were examined.[8] As discussed therein, a number of workers have investigated the use of the Be^{2+} cation as a "fixing agent" for He. In recent work on Be^+–RG complexes (where RG = rare gas),[9] we found that the interaction led to sp hybridization of the Be^+ orbitals, leading to a lowering of electron density along the internuclear axis in the direction of the incoming RG atom. In turn, this led to a reduction in the electron repulsion between the electrons on RG and the unpaired 2*s* electron on Be^+, and a partial exposure of the Be^{2+} core leading to increased attractive terms; a similar picture occurred for Mg^+–RG.[9] For the heavier M^+–RG (M = Ca–Ra) complexes, *sd* hybridization occurred, where electron density could be moved off axis (see Sec. IV A), exacerbating both the reduction in electron repulsion and the increase in attractive terms.[10,11] In the present work, we investigate the binding of He to the HM^+ species, where M is a Group 2 metal.

We also note that, since it contains only light elements, BeH^+ may be of importance in astrochemistry, and its possible dissociative recombination in the interstellar medium (ISM) has been investigated.[12] The amount of helium around in the interstellar medium, together with the very low temperatures, suggests that helium complexation may be present[1] and may be a means for the rotational cooling of ions and neutrals in space; we note the study on the HCa–He complex,[13] which emphasised the use of helium as a means of obtaining ultracold molecules for a number of terrestrial applications. Additionally, ion doping of helium nanodroplets[14] is a plausible way of growing novel materials and understanding the interactions of helium with the dopant ions is an important first step for a full understanding of such processes. Lastly, we also note that interest in the β^- decay of the monotritiated species, HBeT, has been expressed, whose product is HBe^+–He.[15]

To understand the interactions of He with the HM^+ ions, it is necessary to understand the bare ions also. Spectroscopic studies on HBe^+ have been few, with early UV spectra reported by Bengtsson-Knave[16] and Watson and Humphreys[17] yielding rotational and vibrational constants. More-precise values have been reported by Coxon and Colin in 1997.[18] Similarly, there have been limited studies on HMg^+, with the analyses of the early emission spectra of Pearse,[19] Guntsch,[20] and Pillow[21] being refined in the work of Balfour.[22] Again, these have allowed rotational and vibrational constants to be derived, as well as the dissociation energy. No experimental data appear to exist for any of the species HCa^+–HRa^+, except for the dissociation energies of HCa^+, HSr^+, and the deuterated species, DBa^+, which have been reported in a series of papers by Armentrout and co-workers.[23–25]

a)Author to whom correspondence should be addressed. Electronic mail: Tim.Wright@nottingham.ac.uk

Although there have been a number of early quantum chemical studies on HBe^+, Koput's recent Multi-Reference-Averaged Coupled Pair Functional (MR-ACPF) study[26] is the most reliable, and so we compare to those values herein; notably, those values were in excellent agreement with the experimental values reported in Ref. 18. Two recent sets of high-level calculations have been reported for HMg^+: those employing the CIPSI (configuration interaction perturbing a multiconfigurational zeroth-order wave function selected iteratively) method, by Aymar *et al.*[27] from which we select the results using the largest basis sets; and those by Abe *et al.*,[28] from which we select the non-relativistic CCSD(T)/cc-pCV5Z values to which to compare, since we believe these are the most reliable (noting that the relativistic correction made very little difference to the calculated spectroscopic constants in that work). For HCa^+, again we compare with the non-relativistic CCSD(T)/cc-pCV5Z values from those reported in Ref. 28, and the CIPSI values from Aymar and Dulieu.[29] Finally, for HSr^+ and HBa^+, we compare our results to the CCSD(T)/ANO-RCC results of Ref. 27, where basis sets are atomic natural orbitals, which have been designed to be relativistic and correlation consistent. We shall compare our calculated values to these sets of data in Sec. III A.

Several studies on HM^+–He complexes have been undertaken relatively recently. In 2007, Page *et al.*[30] performed high-level, CCSD(T), and MRCI, quantum chemical calculations on HBe^+–He, employing aug-cc-pVQZ basis sets. They found the complex to be linear, with a high dissociation energy of 3010 cm^{-1}, although this was not remarked upon. Separately, but in the same year, similar calculations on the HMg^+–He and HCa^+–He complexes were reported.[31] For the former, again a linear geometry was reported, but with a significantly lower binding energy of 650 cm^{-1}. In contrast, HCa^+–He was found to be bent, with an equilibrium bond angle of $\sim 113^\circ$ and a barrier to linearity of ~ 115 cm^{-1}; its binding energy was found to be 340 cm^{-1}. Although the very different equilibrium geometries were noted in Ref. 31, an explicit, detailed discussion was not given.

In the present work, we investigate the whole HM^+ and HM^+–He series in order to ascertain the geometries, as well as the interaction energies of the latter. We shall also seek to gain insight into the interactions occurring by considering contour plots of the natural orbital density and population analyses.

II. CALCULATIONAL DETAILS

Geometry optimisations of HM^+ and the HM^+–He complexes (where M = Be–Ra) were performed using both MOLPRO[32] and the Gaussian 09[33] suites of programs. We employed MP2 theory for the whole set of species; in addition, as a test of the reliability of the MP2 geometries, optimizations were carried out for the HM^+–He complexes using QCISD theory for the lighter species with M = Be–Ca. Harmonic frequencies were calculated using MP2 theory. Single point CCSD(T) energy calculations were also then carried out at the MP2 equilibrium geometries of all species to obtain more accurate interaction energies; all T_1 diagnostic values[34] were < 0.02 indicating little multireference character. In each case the only electrons not included in the correlation procedure were the 1*s* orbitals of beryllium and magnesium, and any electrons described by an effective core potential (ECP) — see below. Regarding the electronic states, the HM^+ species are all closed-shell singlets ($^1\Sigma^+$), while the HM^+–He complexes are also closed shell, with the state depending on the geometry ($^1\Sigma^+$ for linear, $^1A'$ for bent).

For hydrogen, helium, and beryllium, the basis sets employed were the Dunning-type aug–cc–pVQZ ones;[35,36] for magnesium we employed the aug-cc-pwCVQZ basis set,[37] which employs weighted core-valence functions. For Ca, Sr, Ba, and Ra we employed the aug–cc–pwCVQZ-PP valence basis sets, in conjunction with the small-core, fully relativistic ECP10MDF, ECP28MDF, ECP46MDF, and ECP78MDF effective core potentials, respectively.[38,39] For additional analyses, corresponding triple-ζ basis sets were employed. These comprised natural orbital contour plots of the natural orbital density calculated at the QCISD level of theory in MOLPRO, employing MOLDEN[40] for the visualization. Charge analysis was also undertaken at the QCISD level with Mulliken,[41] natural population analysis (NPA)[42] using the NBO 6.0 code,[43] and Bader's atoms-in-molecules, AIM,[44] method, with the latter being performed with AIMAll.[45] For simplicity, we shall refer to basis sets as aTZ, aQZ or a5Z as appropriate.

III. RESULTS

A. HM^+

The calculated equilibrium bond lengths of the HM^+ molecules are given in Table I, where our results are compared to the previous experimental and highest-level quantum chemical results, briefly noted above. As may be seen, generally the agreement is very good for all parameters. Regarding HBe^+, given the very large basis set employed by Koput,[26] the agreement with our MP2/aQZ results is excellent; the close agreement to the experimental values for both R_e and ω_e is noteworthy. With regard to D_e, our CCSD(T)/aQZ results are in very good agreement with the MR-ACPF/aug-cc-pV7Z(i) results of Koput for BeH^+ (perhaps suggesting the experimental value is not so reliable). For HMg^+ and HCa^+, the agreement of our MP2/aQZ results with the CCSD(T)/cc-pV5Z ones of Ref. 28 is slightly better than with the CIPSI ones,[27] which employed a smaller basis set. Interestingly, for HSr^+ and HBa^+, the agreement with the CIPSI results[27] is slightly better for ω_e than the CCSD(T)/ANO-RCC ones,[27] although our R_e values agree better with those from the latter calculations. For the heavier species, generally the agreement for D_e is better with the CCSD(T)/ANO-RCC results.[27] Our results for HRa^+ appear to be the first such published.

There have been experimental values for D_0 reported for MgH^+, CaH^+, SrH^+, and BaD^+ by Armentrout and coworkers,[23–25] which we have corrected to D_e values in Table I by making use of our ω_e values (suitably adjusted in the case of BaD^+). As may be seen, within the sizeable error bars, the agreement between the calculated values and the experimental ones is reasonably good.

TABLE I. Calculated parameters of the HM^+ molecules at the MP2/aQZ level of theory. See text for full descriptions of basis sets.

	Previous	R_e (Å)	D_e (cm^{-1})	ω_e (cm^{-1})
HBe^+	Present work	1.307	25 550	2275
	MR-ACPF/aug-cc-pV7Z(i)[26]	1.310	25 740	2222
	Expt.[18]	1.310	26 285	2222.2
HMg^+	Present work	1.637	16 840	1789
	CIPSI[27]	1.65	16 380	1599
	CCSD(T)/cc-pV5Z[28]	1.653	16 890	1706
	Expt.[22]	1.652	16 900	1699
	Expt.[24]		16 500 ± 500[a]	
HCa^+	Present work	1.877	17 830	1558
	CIPSI[27]	1.87	17 970	1453
	CCSD(T)/cc-pV5Z[28]	1.896	18 110	1503
	Expt.[23]		16 700 ± 1000[b]	
HSr^+	Present work	2.020	17 200	1448
	CIPSI	1.97	18 080	1429
	CCSD(T)/ANO-RCC[28]	2.041	17 110	1409
	Expt.[24]		18 200 ± 500[a]	
HBa^+	Present work	2.123	20 020	1350
	CIPSI[27]	2.08	21 600	1368
	CCSD(T)/ANO-RCC[28]	2.139	19 760	1477
	Expt.[c]		20 600 ± 800[c]	
HRa^+		2.226	16 390	1299

[a] D_e values obtained from experimental D_0 value from Ref. 24 and corrected to D_e using our ω_e values.
[b] D_e value obtained from experimental D_0 value from Ref. 23 and corrected to D_e using our ω_e value.
[c] D_e value obtained from experimental D_0 value for BaD^+ from Ref. 25 and corrected to D_e using appropriate scaling of our ω_e value.

In summary, the agreement between our results and quite high-level calculations (and limited experimental data) is very satisfactory and suggests MP2/aug-cc-pVQZ calculations are adequate for these species.

B. HM^+–He

The calculated equilibrium geometries of the HM^+–He complexes are reported in Table II. First we note that there is very little difference between the geometries calculated using the MP2 and QCISD methods for the lightest three species, with the M–He bond length being slightly more sensitive than the H–M one. As a consequence, for the heavier species we are confident that the MP2 geometries are reliable. We immediately see that the two lightest species, HBe^+–He and HMg^+–He are calculated to be linear, and that the heavier species are all calculated to be bent. This is consistent with the linear geometries calculated for HBe^+–He and HMg^+–He

TABLE II. Calculated equilibrium geometries, harmonic vibrational frequencies (cm^{-1}), and $HM^+ \ldots He$ dissociation energies (cm^{-1}) of the HM^+–He complexes at the MP2/aQZ and QCISD/aQZ levels of theory. See text for full descriptions of basis sets. Values in square brackets are calculated employing the same basis sets, but at the QCISD level. D_e values have been calculated at the CCSD(T) level of theory using the indicated basis sets, but at the MP2/aQZ optimized geometry. The calculated R_e values for the HM^+ complexes from Table I have been included here for ease of comparison.

							D_e ($HM^+ \ldots He$)		
	R_{M-H} (Å)	R_{M-He} (Å)	θ (deg)	ω_{bend}	ω_{M-He}	$\omega_{M—H}$	aQZ	a5Z	a5Z+CP
HBe^+	1.307					2275			
HBe^+–He	1.299 [1.304]	1.523 [1.527]	180 [180]	232[a]	611	2343	2971	2971	2964
HMg^+	1.637					1789			
HMg^+–He	1.635 [1.648]	2.132 [2.154]	180 [180]	80[a]	233	1808	689	686	676
HCa^+	1.877					1558			
HCa^+–He	1.876 [1.894]	2.553 [2.566]	110 [113]	111	162	1567	394	399	391
HSr^+	2.020					1448			
HSr^+–He	2.020	2.757	102	83	138	1466	322	325	318
HBa^+	2.123					1350			
HBa^+–He	2.124	2.988	87	55	122	1392	276	274	267
HRa^+	2.226					1299			
HRa^+–He	2.226	3.139	91	92	109	1350	224	223	217

[a] Doubly degenerate.

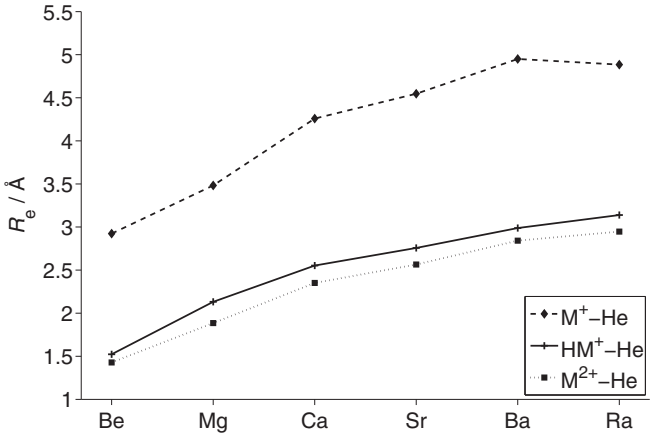

FIG. 1. Plots of the equilibrium bond length for M^+–He, HM^+–He, and M^{2+}–He. See text.

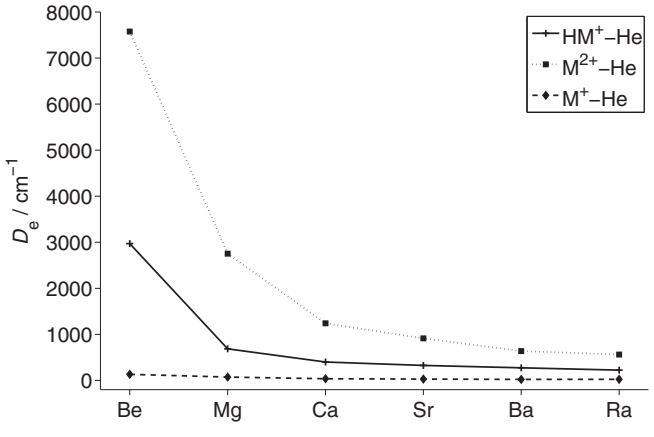

FIG. 2. Plots of the dissociation energy for M^+–He, HM^+–He, and M^{2+}–He. See text.

by Nagy-Felsobuki and co-workers[30] and the bent geometry calculated for HCa^+–He; the results for the three heaviest species appear to be the first published, to our knowledge. In Figure 1 we show the trend of the HM^+–He bond length in these complexes, which can be seen to be monotonically increasing with the atomic number of the metal, in line with general expectations. In Figure 1 we also show the corresponding values for the M^+–He and M^{2+}–He complexes; as may be seen, the HM^+–He values lie in between these, with the values being significantly closer to the dication values than the monocation ones—see Sec. IV A. It can also be noted that the R_e values for the HM^+ complexes are very close to those of the hydrogen–metal bond lengths in the HM^+–He complexes, suggesting that the interaction of HM^+ with He does not perturb the electronic structure of HM^+ significantly. This observation is supported by the ω_e values, where the ω_e values of the HM^+ species are very close to the highest frequency vibration in the complex, which is largely associated with a metal–hydrogen stretching motion. The magnitude of the ω_e values in the complexes that correspond mostly to a metal–helium stretch indicate that the interaction is sizeable, particularly for HBe^+–He. The trend in this vibration is also monotonically decreasing with the atomic number of the metal centre, in line with expectations based on reduced mass, but also in line with the decreasing M…He interaction energies, discussed in Sec. IV C. The trend in the bending vibration is not so clear cut, with a sharp drop from HBe^+–He to HMg^+–He (with the bending mode being doubly degenerate for these two linear complexes); the small rise between HMg^+–He and HCa^+–He can be attributed to a change in the mode of interaction (cf. the change in equilibrium geometry)—see Sec. IV A. There is then a fall through HCa^+–He to HBa^+–He in line with reduced mass and decreasing strength of interaction and then a final rise when moving to HRa^+–He, likely attributable to a combination of relativistic and lanthanide contraction effects.

In Figure 2, the trends in D_e for the binding of He to HM^+ are shown, which exhibit a monotonically decreasing trend with the atomic number of M. This is straightforwardly attributed to the increasing size of M with atomic number, despite the changing nature of the interaction. As with the R_e values, we find the HM^+–He values lie between those of M^+–He and M^{2+}–He, but being closer to those of the dication. See Sec. IV A for further discussion.

IV. DISCUSSION

A. Equilibrium geometries and rationalization of bonding motifs

In order to understand the equilibrium bond angles better, it is first necessary to look at contour plots of the highest occupied molecular orbitals (HOMOs) in the HM^+–He complexes; here we employ the QCISD natural orbital density. These are presented in Figure 3 for M^+ = Be and Mg, and in Figure 4 for $M^+ = Ca^+$–Ra^+; in addition, we show the corresponding plots for the HM^+ diatomics in the same figures. It is clear that there is very little difference observed in the electron density on the metal centre between corresponding HM^+ and HM^+–He species, and that for the HM^+–He complexes, there is very little involvement of the He 1*s* orbital—this suggests there is little covalency in these systems. For HBe^+–He and HMg^+–He (see Figure 3), we see that the He atom is interacting with the M^+ core along the same direction as the HM^+ internuclear axis. In the cases of the heavier complexes from HCa^+–He to HRa^+–He (Figure 4), we see that the He atom is now interacting in a position that is just skewed away from perpendicular to the HM^+ internuclear axis. Additionally, it is clear that the form of the HOMOs in Figure 4 is different to those in Figure 3.

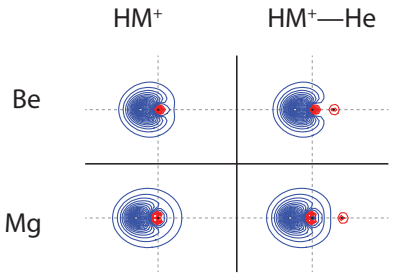

FIG. 3. Contour plots of the QCISD/aTZ natural orbital density for HM^+ and HM^+–He (M = Be, Mg).

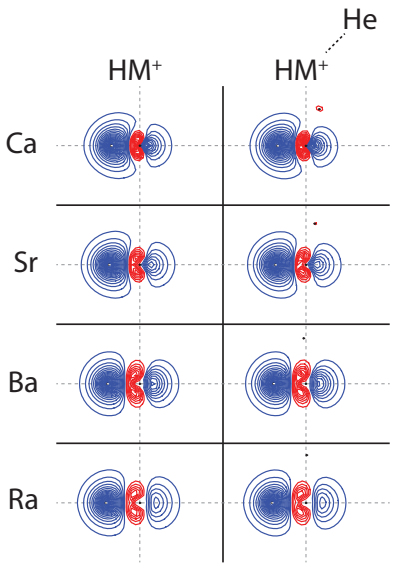

FIG. 4. Contour plots of the QCISD/aTZ natural orbital density for HM^+ and HM^+–He (M = Ca–Ra).

In Table III we show the results of NBO analyses of the QCISD density for both HM^+ and HM^+–He. These clearly show that the lightest two pairs of species have small amounts of *sp* hybridization on the M^+ centre, while all of the heavier ones have more significant amounts of *sd* hybridization, with a very small amount of *p* character. For M = Be and Mg, it is clear that the majority of the σ HOMO is formed between the H 1*s* orbital and the outermost *s* orbital on the metal centre; however, the small amounts of *sp* hybridization are enough to locate the He in its observed position. The more significant amounts of *sd* hybridization for the heavier metals is evident from the population analyses and is seen clearly in the contour plots (see Figures 3 and 4). It is noteworthy that for HBa^+, although the HOMO is predominantly H 1*s* in nature, the largest contribution from barium is that of the $5d_z^2$ orbital, rather than the 6*s* orbital into contrast to the HOMOs of the other heavy species where the contribution from the outermost s orbital is the larger. Since the He atom is so weakly bound, it is an extremely sensitive probe of the electron density, and its equilibrium position is strongly influenced by the form of the electron density. Essentially, the hybridization occurs as a result of the formation of the HM^+ bond, with only very minor modifications made by the He atom, which just experiences the form of the HM^+ electron density. Thus, this is in line with the conclusions from the contour plots described above, that there is essentially no covalency in the HM^+...He interactions—even for HBe^+–He, which has a substantial binding energy. We can also see that the predominant contribution from the hydrogens is the 1*s* orbital, with small contributions from other orbitals.

If we now look at the population analyses in Table IV, we see that the Mulliken analysis gives a charge of only +0.75*e* on the Be centre in HBe^+–He, while the NPA and AIM approaches give higher charges, with a value of +1.75*e* using AIM; similar comments apply to HMg^+–He. These differences are still present for the heavier species, HM^+–He (M^+ = Ca^+–Ra^+) but become less pronounced; additionally, we note that the charges on the metal centre have plateaued for these heavier species. In Figure 1, we show the calculated H–M^+–He internuclear separations, alongside those for the M^+–He and M^{2+}–He complexes, calculated in our previous work.[9–11] From these it is clear that the calculated separations in HM^+–He are much closer to those of the dications than the monocations, in line with the calculated NPA and AIM charges, with the AIM ones being most in line. We also note that the NPA charge of +0.06*e* on the He atom in HBe^+–He is not in line with the contour plots, and so we conclude that the AIM analysis appears to be the most reliable of the three

TABLE III. NBO data for the H–M^+ HOMO bonding orbital calculated from the QCISD/aTZ natural orbital density for the HM^+ and HM^+–He series. In cases where the totals of the shown numbers are slightly less than 100%, there are small contributions from higher angular momentum functions.

	Overall atomic contributions		Contributions from H orbitals		Contributions from M orbitals		
	% H	% M	% H *s*	% H *p*	% M *s*	% M *p*	% M *d*
HBe^+	73.7	26.3	97.1	2.8	91.1	8.8	0.1
HBe^+–He	74.5	25.5	97.0	3.0	90.5	9.4	0.1
HMg^+	74.4	25.6	98.0	2.0	98.3	1.5	0.2
HMg^+–He	75.9	24.1	97.7	2.2	98.1	1.7	0.2
HCa^+	86.0	14.0	98.5	1.5	69.8	0.4	29.6
HCa^+–He	86.3	13.7	98.4	1.6	69.0	0.4	30.5
HSr^+	87.6	12.4	98.8	1.2	63.1	0.3	36.4
HSr^+–He	87.8	12.3	98.7	1.3	62.7	0.3	36.8
HBa^+	88.8	11.2	98.9	1.1	28.4	0.6	70.0
HBa^+–He	88.8	11.2	98.8	1.2	29.2	1.0	68.7
HRa^+	88.7	11.3	98.9	1.1	54.9	1.0	42.7
HRa^+–He	88.8	11.2	98.8	1.2	55.0	1.5	42.1

TABLE IV. Calculated atomic charges and $H(R)$ values at the QCISD/aTZ//MP2/aQZ level—see text for full basis sets and details.

		HBe^+–He	BeH^+	HMg^+–He	MgH^+	HCa^+–He	CaH^+	HSr^+–He	SrH^+	HBa^+–He	BaH^+	HRa^+–He	RaH^+
Mulliken	M	0.75	0.72	0.97	0.96	1.29	1.27	1.46	1.45	1.54	1.54	1.51	1.51
	H	0.26	0.28	0.08	0.04	−0.27	−0.27	−0.45	−0.45	−0.54	−0.54	−0.51	−0.51
	He	−0.01		−0.05		−0.02		−0.01		−0.01		0.00	
NPA	M	1.43	1.46	1.49	1.47	1.71	1.71	1.74	1.74	1.76	1.76	1.76	1.76
	H	−0.49	−0.46	−0.50	−0.47	−0.71	−0.71	−0.74	−0.74	−0.76	−0.76	−0.76	−0.76
	He	0.06		0.02		0.01		0.00		0.00		0.00	
AIM													
	M	1.75	1.72	1.56	1.53	1.65	1.65	1.67	1.66	1.64	1.64	1.67	1.67
	H	−0.76	−0.72	−0.56	−0.53	−0.66	−0.65	−0.67	−0.66	−0.65	−0.64	−0.68	−0.67
	He	0.01		0.00		0.00		0.00		0.00		0.00	
$H(R)$	$M^+ \ldots H$	−0.056	−0.050	−0.012	−0.012	−0.020	−0.020	−0.019	−0.019	−0.022	−0.023	−0.017	−0.017
	M^+–He	0.012		0.005		0.003		0.003		0.002		0.002	

methods employed here—a result in line with our conclusions in work on the Be^+–RG_2 and Mg^+–RG_2 complexes,[46] and also work on the MH^- species.[47] We can also see that a charge close to $2e$ on the M centre is more reasonable for the calculated D_e values and their comparison to those for M^+–He and M^{2+}–He presented in Figure 2; as with the R_e values, these are much closer to the values obtained for M^{2+}–He, than they are for M^+–He. Thus, in line with the conclusions of other workers,[1,8] the charge on the binding site of the helium is a dominant parameter in providing high interaction energies.

In the contour plots in Figure 3, we can see that for the beryllium- and magnesium-containing species, the *s* orbital (containing a small amount of *sp* hybridization) on the M centre overlaps with the 1*s* orbital on H to form a σ bond. This gives a covalent H–M^+ bond, as may be seen from the negative value of the total local energy density, $H(R)$,[48] reported in Table IV; in contrast, the positive values of $H(R)$ are consistent with the non-covalent nature of the interaction with the He atom, as concluded above. Upon formation of the σ bond, the electron density is reduced on the side opposite the H atom, favouring an approach by the He atom in this location, as observed (see Figure 3). These ideas are related to the donor-acceptor ideas discussed in Ref. 1.

For the heavier species, the formally unoccupied *d* orbitals on the M centre are significantly lower in energy, and small amounts of *sd* rather than *sp* hybridization is the main observation (see Table III). The *sd* hybrid is formed with the d_z^2 orbital, and in a fashion such that the lobes of the d_z^2 orbital have the same phase as the *s* orbital and this leads to a build-up of electron density in the lobal regions. One of the *sd* hybrid orbital lobes then interacts with the H 1*s* orbital to form the covalent H–M σ bond, with the covalency indicated by the negative values of $H(R)$—see last rows of Table IV; the positive values of $H(R)$ for the M…He region indicate no such covalency. Concomitant with the build-up of electron density in the global regions, there is an out-of-phase interaction of the central "torus" of the d_z^2 orbital, which leads to a reduction in electron density perpendicular to the H–M internuclear axis. Because of the isotropic nature of the s electronic wavefunction and the form of the d_z^2 orbital, there are curved nodal surfaces formed upon hybridization along paths where the *s* and *d* electron density just cancel: effectively the torus becomes distorted, and this is exacerbated by repulsion from the hydrogen–metal σ bond electron density.

The helium atom will be positioned such that it benefits from the most energetically favourable balance of attractive and repulsive effects. The attractive energy is expected to be dominated by charge-induced dipole interactions, and so the He atom is expected to try and locate itself as radially close to the metal nucleus as possible to maximize this, but also at an angular position that facilitates its exposure to the partially exposed M^{2+} core. The counterbalance to this will be electron repulsion interactions, which will be particularly pronounced in linear orientations, but with non-equal repulsions from the two regions of high electron density, owing to the formation of the H–M σ bond. These considerations explain why the He atom is located in a position close to perpendicular for the heavier species (see Figure 4) but is slightly displaced away from this position in HCa^+–He and in the heavier species. Note that the He atom will also have an attractive charge/induced-dipole interaction with the negative H part of the HM^+ molecule, but the magnitude of this interaction will be much smaller, both due to the large distance R from the hydrogen, and the fact that the magnitude of the charge on H is smaller than e, while for the metal it close to $+2e$ (with the terms being proportional to square of the charge).

B. Angular plots

We now discuss the angular plots presented in Figure 5, where we have selected two systems: HBe^+–He and HBa^+–He, as the "most *sp* hybridized" and the "most *sd* hybridized," respectively. The left-hand plots (a)–(c) show the energy relative to the $HM^+ \ldots$ He dissociation asymptote, where the bond lengths have been optimized at each angle, and so these curves represent a minimum-energy path of the helium atom around the HM^+ cation. The plot in Fig. 5(c) is a zoomed-in region of the relative energy plot for HBa^+–He shown in Fig. 5(b).

From Fig. 5(a) it can be seen that the potential energy surface for HBe^+–He is close to isotropic around the H end (0°) of the HBe^+, with a steep minimum as the He atom moves towards linearity on the M^+ end of the molecule (180°). Somewhat similarly, in HBa^+–He, see Fig. 5(b), there is a

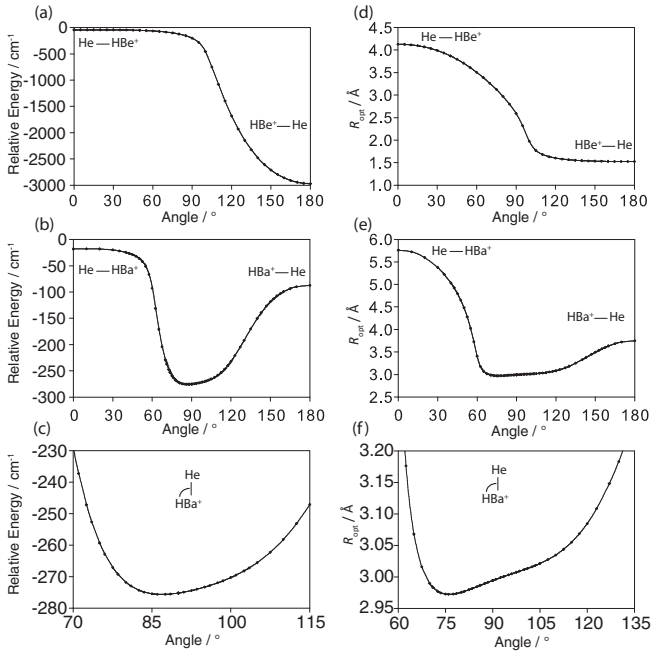

FIG. 5. Angular potential plots for HBe^+–He and HBa^+–He. The left-hand plots show the energy relative to the appropriate HM^+ + He dissociation asymptote; at each angle the bond lengths have been optimized. The right-hand plots show the optimized value of the metal–helium bond distance at each angle (the metal-hydrogen bond distance has also been optimized). The bottom two traces are expanded views of the middle two traces.

region that is close to isotropic on the H end of HBa^+, but this is much narrower than in HBe^+–He, which is due to the nonlinear minimum. There is then a very steep drop to the minimum close to 90°, before another steep rise (but not quite as steep as the initial drop) to the local maximum at 180°. The unusually shaped well is attributable to the form of the electron density of the distorted torus in the region close to 90°, coupled with the asymmetry in the heights of the maxima; the zoomed-in region in Fig. 5(c) shows this asymmetry more clearly.

In the right-hand graphs (Figs. 5(d)–5(f)), we have plotted the optimized value of R(M^+–He), R_{opt}, against bond angle. For HBe^+–He (Fig. 5(d)) the plot shows that this distance falls sharply from 0° (corresponding to He…HBe^+), as the He atom becomes able to interact more strongly with the beryllium centre; it is interesting to note that the bond length then remains close to constant, albeit dropping slowly as linearity (HBe^+…He) is approached. Similar behaviour is seen for the small angles for HBa^+–He (Fig. 5(e)), with again the sharp fall in this distance from the maximum at 0° (He…HBa^+) as the H atom is navigated. The minimum R_{opt} value now occurs at an angle close to perpendicular, with a subsequent rise until bond angles close to 120°, when there is then a sharper rise, before a slight plateau at 180° (HBa^+….He). In Fig. 5(f) we show an expanded view of the region close to the potential energy minimum; as expected, this region of strongest interaction yields the shortest R_{opt} values. It is interesting to note that the lowest R_{opt} value is at ∼75°, while the potential minimum is at 87°, which is initially surprising; however, the explanation lies in the minimum being determined by a balance between attractive and repulsive effects, which each have different R dependences. As a consequence, there is no reason for the global potential energy minimum to correspond to the lowest value of R_{opt}.

We note that in Ref. 31, the barrier to linearity for the HCa^+–He complex was calculated as 115 cm^{-1}, while in the present work a value of 172.7 cm^{-1} from RCCSD(T)/a5Z calculations was obtained. As may be seen, our value is significantly different to that in Ref. 31, which also employed the CCSD(T) method; however, we note that although similar basis sets were employed for H and He in that work, for calcium a smaller, non-ECP, basis set was employed, and this may be the source of the discrepancy.

We now consider these angular potential plots and the contour plots shown in Fig. 4. It may be seen that in the bottom plot in Fig. 5, there is an initial clear rise in the R_{opt} value, but then there is a lessening of the gradient before it begins to rise more steeply again. Looking at the contour plots in Fig. 4, for HBa^+–He, it may be seen that this region close to perpendicular is where the He atom is moving across the electron density of HBa^+ associated with the torus region of the *sd* hybrid.

Overall, the plots in Fig. 5 confirm that the interaction with He is a sensitive probe of the shape of the electron density around the HM^+ molecule.

C. Magnitude of binding energies

In Table V, we have tabulated both the equilibrium M…He bond lengths and the binding energies of the HM^+–He complexes from the present work and those for the M^+–He and M^{2+}–He complexes from our previous work; these are the data that are plotted in Figures 1 and 2. We have also calculated two ratios: $D_e(HM^+–He)/D_e(M^+–He)$, which we have denoted by D_e ratio$^+$ in Table V; and

TABLE V. Calculated equilibrium bond lengths (Å) and dissociation energies (cm^{-1}) and ratios for M^+–He, HM^+–He, and M^{2+}–He, as used in Figures 1 and 2. See text for references of values not calculated in the present work. Dissociation energy ratios are defined in the table footnote.[a]

	$R_e(M^+–He)$	$R_e(M^{2+}–He)$	$R_e(HM^+–He)$	D_e (M^+–He)	$D_e(HM^+–He)$	D_e ratio$^+$	$D_e(M^{2+}–He)$	D_e ratio^{2+}
Be	2.924	1.428	1.527	133	2964	22.3	7575	0.39
Mg	3.482	1.885	2.154	73	676	9.3	2753	0.25
Ca	4.259	2.351	2.566	36	391	10.9	1240	0.31
Sr	4.547	2.565	2.757	29	318	11.0	914	0.35
Ba	4.950	2.842	2.988	22	267	12.1	638	0.42
Ra	4.885	2.947	3.139	23	217	9.4	562	0.39

[a]D_e ratio$^+$ is the ratio $D_e(HM^+–He)/D_e$ (M^+–He). D_e ratio^{2+} is the ratio $D_e(HM^+–He)/D_e(M^{2+}–He)$.

$D_e(HM^+–He)/D_e(M^{2+}–He)$, which we have denoted D_e ratio^{2+}. Looking first at the D_e ratio$^+$ values, we see that the values are remarkably stable with a value around 10, except for HBe^+–He, where the ratio is about twice the other values. In contrast, the D_e ratio^{2+} values are much closer, with values around 0.3–0.4, although the HMg^+–He value is a little lower than the others. Although we have not presented any ratios, it is clear that for the R_e values, those for HM^+–He are each closer to the corresponding M^{2+}–He values than for the M^+–He values, as noted above (see Fig. 1).

To rationalize the sets of D_e ratio values, we first note that the close-to-constant values for D_e ratio^{2+} suggest that, even though two different hybridization schemes are present, the hybridization and subsequent σ bonding for all of the HM^+ species leads to a close-to-constant exposure of the M^{2+} core on the side opposite to H. Since we expect charge-induced dipole terms to dominate the attractive interactions, this would suggest that the effective charge of the M centre should be about constant, and the values in Table IV indicate that this is the case, with all values in the approximate range 1.6 *e*–1.7*e*. If we now look back at the D_e ratio$^+$ values, we might expect a similar constancy as for the D_e ratio^{2+} values, but as noted, the value for HBe^+–He is significantly higher. This is mostly due to the R_e values, with the relevant R^4 ratios also showing the same anomaly for beryllium. A reasonable explanation for this is that in Be^{2+}–He and HBe^+–He, where there is little 2*s* electron density, the He atom can get close to the (hard) beryllium cation; in Be^+–He the 2*s* electron density prevents the He from approaching as closely. The He atom cannot get as close for the other metals considered here, as there are occupied *p* orbitals in the dication, which serve to increase the electron repulsion, since there is electron density in the highest occupied p_z orbital.

To consider these ratios further, we examined the charge/induced-dipole interactions in the HM^+–He complexes in more detail. For the two linear species, HBe^+–He and HMg^+–He, this is relatively straightforward. The metal cation induces a dipole on the He, with a magnitude dependent on the polarizability of He, the effective charge on the metal centre and the inverse of the square of the distance of M from He; contemporaneously and with corresponding dependences, the H^- also induces a dipole, but in the opposite direction; these two induced dipoles add vectorially to give the overall induced dipole. To obtain the total charge/induced-dipole binding energy, the interaction of the overall dipole with each of the respective charged centres needs to be calculated, with the sum giving the overall charge/induced-dipole interaction energy. For the nonlinear case a similar procedure is undertaken, with the respective dipoles again being added vectorially. In Table VI we tabulate these values. First, it can be seen that the values of the ratios are very close to the D_e ratio^{2+} values in Table V. This may at first be surprising, since the D_e values will contain higher-order attractive terms, as well as repulsion terms. In addition, for the heavier species, the $D_e(HM^+–He)$ values are very close to the V_{ind}(sum) values, suggesting either that the repulsion and higher-order terms are both small, or that they fortuitously balance out. The fact that the agreement is less good for the lighter complexes perhaps suggests the latter, with the HBe^+–He and HMg^+–He species expected to have less electron repulsion, since the negatively charged H atom is much further away from the He atom than it is with the bent species.

TABLE VI. Calculated charge/induced-dipole energies (cm^{-1}) for the HM^+–He complexes, calculated at the MP2/aQZ optimized geometries (see Table II), and employing the AIM charges (see Table IV).

	V^{ind}(M)	V^{ind}(H)	V^{ind}(sum)	$D_e(HM^+–He)$	$V^{ind}(M^{2+}–He)$	Ratio[a]
Be	5929	− 740	5189	2964	11 450	0.45
Mg	1241	− 147	1098	676	3771	0.29
Ca	634	− 100	534	391	1558	0.34
Sr	468	− 79	389	318	1100	0.35
Ba	313	− 58	255	267	730	0.34
Ra	268	− 50	218	217	631	0.35

[a] V^{ind}(sum)/$V^{ind}(M^{2+}–He)$—this is the equivalent of D_e ratio^{2+}, as presented in Table V. See text for further details.

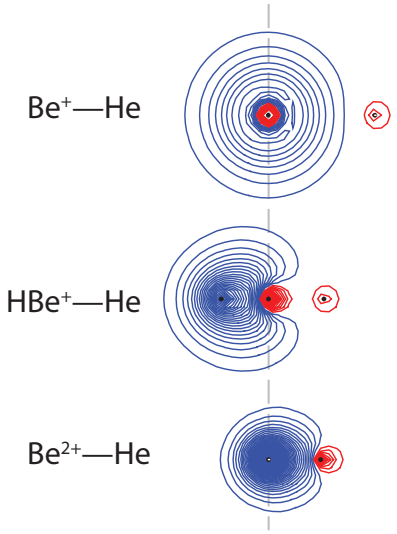

FIG. 6. Contour plots of the QCISD/aTZ natural orbital density for Be^+–He, HBe^+–He, and Be^{2+}–He.

We emphasise that all of the above effects could be deemed "physical," in the sense that no significant charge transfer or sharing of electron density is occurring, but noting that the occurrence of hybridization could be deemed a "chemical" effect. This hybridization and formation of the M–H bond in the MH^+ species leads to an increased charge on the M centre, which dominates the interaction. In Figure 6, we show contour plots of the key species for the case of M = Be. It can be seen that the amount of He 1*s* character involved in the bonding is rather small, and actually resembles very closely the Be^+–He contour; we refer the reader to one of our previous papers where we explored the idea of using ion-helium complexes as a means of defining the "size" of an ion.[49] Even in Be^{2+}–He, the amount of involvement of the He 1*s* orbital is small, despite the higher charge and smaller size of the Be^{2+} ion.

V. CONCLUSIONS

We have investigated the bonding in the HM^+–He species for the whole of the Group 2 metals. We have confirmed that the bonding in HBe^+–He is surprisingly strong,

and have rationalized this by the formation of the H–Be^+ σ bond, which removes electron density from the "other" side of Be. This then makes it favourable for the He atom to approach on the side opposite to the hydrogen. Despite the magnitude of the interaction, there is little evidence for chemical bond formation, with the strength of interaction being attributable to the exposure of the M^{2+} core, giving a strong, mainly physical interaction, although it is arguable that hybridization itself can be viewed as a chemical effect. Similar comments apply to HMg^+–He, although the interactions are significantly lower.

For the heavier species, there are formally unoccupied *d* orbitals low in energy, particularly for barium, and this allows the formation of *sd* hybrids, leading to the formation of the σ bond in HBa^+. The form of the molecular orbital is such that there is a small build-up of electron density on the intermolecular axis on the side opposite to the hydrogen, but a reduction in density along an angle close to 90°; this leads to more exposure of the M^{2+} core along this direction. The He atom is thus located in the latter position, at an angle determined by the optimal balance in repulsion and attraction, which is slightly different for each of the heavier species. Various angular plots have shown that the interaction with the He atom is very sensitive to the form of the electron density distribution of HM^+.

ACKNOWLEDGMENTS

The authors are grateful for the provision of computing time by the EPSRC under the auspices of the NSCCS. The EPSRC are thanked for funding (Grant EP/I012303/1) and the provision of a studentship to J.P.H. W.H.B. is grateful to the Department of Chemistry at the University of Utah for travel funding, allowing visits to the University of Nottingham.

[1]W. Koch, G. Frenking, J. Gauss, D. Cremer, and J. R. Collins, J. Am. Chem. Soc. **109**, 5917 (1987).
[2]C. J. Evans, T. G. Wright, and A. M. Gardner, J. Phys. Chem. A **114**, 4446 (2010).
[3]W. Zou, D. Nori-Shargh, and J. E. Boggs, J. Phys. Chem. A **117**, 207 (2013).
[4]W. L. Zou, Y. Liu, and J. E. Boggs, Chem. Phys. Lett. **482**, 207 (2009).
[5]R. Chen, H. Zhu, D. Q. Xie, and G. S. Yan, Sci. China, Ser. B **52**, 1987 (2009).
[6]X. Wang, L. Andrews, F. Brosi, and S. Riedel, Chem. – Eur. J. **19**, 1397 (2013).
[7]X. Wang, L. Andrews, K. Willmann, F. Brosi, and S. Riedel, Angew. Chem., Int. Ed. **51**, 10628 (2012).
[8]P. Antoniotti, P. Facchini, and F. Grandinetti, Int. J. Mass Spectrom. **228**, 415 (2003).
[9]A. M. Gardner, C. D. Withers, J. B. Graneek, T. G. Wright, L. A. Viehland, and W. H. Breckenridge, J. Phys. Chem. A **114**, 7631 (2010).
[10]M. F. McGuirk, L. A. Viehland, E. P. F. Lee, W. H. Breckenridge, C. D. Withers, A. M. Gardner, R. J. Plowright, and T. G. Wright, J. Chem. Phys. **130**, 194305 (2009).
[11]A. M. Gardner, C. D. Withers, T. G. Wright, K. I. Kaplan, C. Y. N. Chapman, L. A. Viehland, E. P. F. Lee, and W. H. Breckenridge, J. Chem. Phys. **132**, 054302 (2010).
[12]S. Niyonzima, F. Lique, K. Chakrabarti, Å. Larson, A. E. Orel, and I. F. Schneider, *European Conference on Laboratory Astrophysics - ECLA*, EAS Publication Series Vol. 58, edited by C. Stehlé, C. Joblin, and L. d'Hendecourt (Cambridge University Press, 2012), p. 291.
[13]G. C. Groenenboom and N. Balakrishnan, J. Chem. Phys. **118**, 7380 (2003).
[14]See, for example, R. Wesendrup, G. Esperenza Moyano, M. Pernpointner, and P. Schwerdtfeger, J. Chem. Phys. **117**, 7506 (2002).
[15]S. Ikuta, K. Yoshihara, and T. Shiokawa, J. Nucl. Sci. Technol. **14**, 720 (1977).
[16]E. Bengtsson-Knave, Nova Acta Regiae Soc. Sci. Ups. **8**, 1 (1932).
[17]W. W. Watson and R. F. Humphreys, Phys. Rev. **52**, 318 (1937).
[18]J. A. Coxon and R. Colin, J. Mol. Spectrosc. **181**, 215 (1997).
[19]R. W. B. Pearse, Proc. R. Soc. A **125**, 157 (1929).
[20]A. Guntsch, Z. Phys. **107**, 420 (1937).
[21]M. E. Pillow, Proc. Phys. Soc. London Sect. A **62**, 237 (1949).
[22]W. J. Balfour, Can. J. Phys. **50**, 1082 (1972).
[23]R. Georgiadis and P. B. Armentrout, J. Phys. Chem. **92**, 7060 (1988).
[24]N. F. Dalleska, K. C. Crellin, and P. B. Armentrout, J. Phys. Chem. **97**, 3123 (1993).
[25]P. B. Armentrout and J. L. Beauchamp, Chem. Phys. **48**, 315 (1980).
[26]J. Koput, J. Chem. Phys. **139**, 104309 (2013).
[27]M. Aymar, R. Guérout, M. Sahlaoui, and O. Dulieu, J. Phys. B: At., Mol. Opt. Phys. **42**, 154025 (2009).
[28]M. Abe, M. Kajita, M. Hada, and Y. Morikawa, J. Phys. B: At., Mol. Opt. Phys. **43**, 245102 (2010).
[29]M. Aymar and O. Dulieu, J. Phys. B: At., Mol. Opt. Phys. **45**, 215103 (2012).
[30]A. J. Page, D. J. D. Wilson, and E. I. Nagy-Felsobuki, Chem. Phys. Lett. **442**, 194 (2007).
[31]A. J. Page and E. I. Nagy-Felsobuki, Phys. Chem. Chem. Phys. **10**, 1285 (2008).
[32]H.-J. Werner, P. J. Knowles, G. Knizia, F. R. Manby, M. Schütz *et al.*, MOLPRO, version 2012.1, a package of *ab initio* programs, 2012, see http://www.molpro.net.
[33]M. J. Frisch, G. W. Trucks, H. B. Schlegel *et al.*, Gaussian 09, Revision D.01, Gaussian, Inc., Wallingford, CT, 2009.
[34]T. J. Lee and P. R. Taylor, Int. J. Quantum Chem. **36**, 199 (1989).
[35]T. H. Dunning, Jr., J. Chem. Phys. **90**, 1007 (1989).
[36]D. E. Woon and T. H. Dunning, Jr., J. Chem. Phys. **100**, 2975 (1994).
[37]B. Prascher, D. E. Woon, K. A. Peterson, T. H. Dunning, Jr., and A. K. Wilson, Theor. Chem. Acc. **128**, 69 (2011).
[38]I. S. Lim, H. Stoll, and P. Schwerdtfeger, J. Chem. Phys. **124**, 034107 (2006).
[39]M. Kaupp, P. V. R. Schleyer, H. Stoll, and H. Preuss, J. Chem. Phys. **94**, 1360 (1991).
[40]G. Schaftenaar and J. H. Noordik, "Molden: A pre- and post-processing program for molecular and electronic structures," J. Comput.-Aided Mol. Des. **14**, 123 (2000).
[41]R. S. Mulliken, J. Chem. Phys. **23**, 1833 (1955).
[42]A. E. Reed, R. B. Weinstock, and F. Weinhold, J. Chem. Phys. **83**, 735 (1985).
[43]E. D. Glendening, J. K. Badenhoop, A. E. Reed, J. E. Carpenter, J. A. Bohmann, C. M. Morales, C. R. Landis, and F. Weinhold, NBO 6.0, Theoretical Chemistry Institute, University of Wisconsin, Madison, 2013.
[44]R. F. W. Bader, *Atoms in Molecules—A Quantum Theory* (Oxford University Press, Oxford, U.K., 1990).
[45]T. A. Keith, T. K. Gristmill Software, AIMAll, Overland Park, KS, 2011, see aim.tkgristmill.com.
[46]A. Andrejeva, A. M. Gardner, J. B. Graneek, R. J. Plowright, W. H. Breckenridge, and T. G. Wright, J. Phys. Chem. A **117**, 13578 (2013).
[47]J. P. Harris, D. R. Manship, W. H. Breckenridge, and T. G. Wright, J. Chem. Phys. **140**, 084304 (2014).
[48]D. Cremer and E. Kraka, Angew. Chem., Int. Ed. Engl. **23**, 627 (1984).
[49]T. G. Wright and W. H. Breckenridge, J. Phys. Chem. A **114**, 3182 (2010).